EXPERIMENTAL STUDIES TOWARDS UNDERSTANDING AEROMECHANICS OF A FLEXIBLE ROBOTIC HUMMINGBIRD WING IN HOVER

An Undergraduate Research Scholars Thesis

by

KANIKA GAKHAR

Submitted to the Undergraduate Research Scholars program at
Texas A&M University
in partial fulfillment of the requirements for the designation as an

UNDERGRADUATE RESEARCH SCHOLAR

Approved by Research Advisor: Dr. Moble Benedict

May 2017

Major: Aerospace Engineering

TABLE OF CONTENTS

ABSTRACT

Experimental Studies Towards Understanding Aeromechanics of a Flexible Robotic Hummingbird Wing in Hover

Kanika Gakhar
Department of Aerospace Engineering
Texas A&M University

Research Advisor: Dr. Moble Benedict
Department of Aerospace Engineering
Texas A&M University

This study investigated the aeroelastic mechanics of a flexible flapping wing designed and implemented on a two-winged, flapping wing, robotic hummingbird capable of hovering. The investigation focused first on measuring aerodynamic and inertial forces and using these results to quantify efficiency; second, on measuring vertical inertial forces on the flexible flapping wing for the first time using Digital Image Correlation; and three, on quantifying the flowfield using Particle Image Velocimetry at the 70%spanwise location of the wing. The purpose of these experiments was to optimize the lift generation and increase the efficiency of the hover-capable robotic hummingbird. A bench-top experimental setup was designed and developed which flapped a duplicate of the wing used in the actual flying vehicle, and utilized the same flapping kinematics. This setup allowed for the variation of flapping parameters, as well as measurement of performance metrics through sensors which measured the instantaneous lift, torque, flap angle, and current draw. The results found that 108° flapping amplitude at 20 Hz was the most power efficient. This is the first time instantaneous vertical force and torque measurements have been successfully conducted on a flexible, hover capable flapping wing used

on a flying vehicle. Additionally, this study calculates vertical inertial loads for the same type of wing using deflection measurements. Results from this investigation can be used for further refinement and structural tuning of flexible flapping wing design for hovering flight.

ACKNOWLEDGEMENTS

I would like to thank my faculty research advisor, Dr. Benedict, and my graduate research mentor, David Coleman, for their guidance and support throughout the course of this research. I am also very thankful for having access to state of the art equipment and facilities at the Advanced Vertical Lift Flight laboratory.

I would like to express my gratitude towards the Undergraduate Summer Research Grant and Undergraduate Research Scholars programs for providing me with resources to improve my research. I also want to extend my gratitude to the Department of Aerospace Engineering at Texas A&M University for giving me opportunities to grow and learn as an undergraduate research assistant.

Finally, I am sincerely appreciative of the support and encouragement given to me by my mother and father.

NOMENCLATURE

C_L	Coefficient of Lift
C_{avg}	Average Current drawn by motor during one cycle
$C(r)$	Chord Length of the Wing as a function or Radial Distance
C_{max}	Maximum Chord Length of the Wing (along Vertical Spar)
dr	Incremental Radial Distance along the Leading Edge of the Wing
E	Efficiency of Flapping Mechanism
f	Flapping Frequency of Wing for one cycle
GR	Gear Ratio between Reduction Gear and Pinion Gear
J	Second moment of Area of the Wing
L_{avg}	Average Lift generated by wing at an instant in time
m_1	Slope of Trailing Edge connecting end of Vertical Spar and Diagonal Spar
m_2	Slope of Trailing Edge connecting end of Diagonal Spar and Horizontal Spar
P_{out}	Mechanical Output Power produced by Motor
P_{in}	Electrical Input Power drawn by Motor
r	Radial Distance along the Leading Edge of the Wing
ρ	Air Density
T_{avg}	Average Torque acting on motor during one cycle
V_{avg}	Average Angular Velocity of wing at an instant in time
V_{in}	Input Voltage from power supply during one cycle
WS_1	Wing Span of First Segment (from tip of Vertical Spar to Diagonal Spar)
WS_2	Wing Span of Second Segment (from tip of Diagonal Spar to Horizontal Spar)

CHAPTER I

INTRODUCTION

Birds and insects with flapping wings have fascinated humans from the beginning of time. However, scientists and engineers have struggled with understanding the true physics involved especially in hover-capable flapping flight, and how to efficiently replicate such high-frequency flapping wing motion most efficiently. From the aerodynamic forces responsible for creating lift and thrust, to the inertial loads transferred through high-frequency flapping wing motions, there are several factors that play a crucial role in generating hovering flight, but are nonetheless, sparsely understood. What is known, is that flapping wing flight provides remarkable gust tolerance and agility (Ref. 1), and that flapping wings generate extremely high instantaneous coefficients of lift when compared to fixed wings or rotor blades (Ref. 2 and 3). For these reasons, there have been many micro-aerial vehicles designed and developed today which are based on nature-inspired mechanisms and biomimicry.

Current Small-Scale Aerial Robots

A few research teams have successfully designed and developed various types of flapping wing aerial vehicles in the past; however, these designs either do not truly emulate hummingbird-like flight, which is of most interest due to its superior flying abilities, or are very complex machines. For example, the RoboRaven (Ref. 4) from University of Maryland and Smartbird (Ref. 5) by Festo are ornithopters and require forward motion in order to generate lift. Moreover, the DelFly (Ref. 6) from Delft University and the Techject (Ref. 7) from Georgia Tech University rely on four-flapping wings and additional control surfaces. The Nano

Hummingbird (Ref. 8) by AeroVironment, while closely mimicking an actual hummingbird, utilizes a mechanically intricate mechanism and sustains a very small payload. Additionally, its control methodology utilizes techniques that change the wing properties, rather than modulate the wing kinematics, as is seen in natural flyers.

Texas A&M's Robotic Hummingbird

The next generation of aerial robots requires novel breakthroughs to develop concepts which are compact, efficient, hover, and high-speed capable, with generate lower acoustic signatures. Hence, Texas A&M's Advanced Vertical Flight team has designed, built, and flown a truly biomimetic two-winged, hover-capable, robotic hummingbird (Ref. 9) that is mechanically simplistic, utilizes wing kinematic modulation techniques for control and stabilization, and is larger, permitting a larger payload capacity. As described in reference 9, the current Robotic Hummingbird (Figs. 1 and 2) prototype has a 12-inch wingspan, flaps at about 22 Hz, and weighs about 62 grams. This robotic hummingbird uses an extended 4-bar crank rocker or "modified 5-bar" mechanism for large flap sweep with a mean amplitude of 110 degrees. Such a large sweep area is necessary for hovering flight in order to decrease the flapping frequency and disk loading, and increase the total thrust generated. Every load bearing

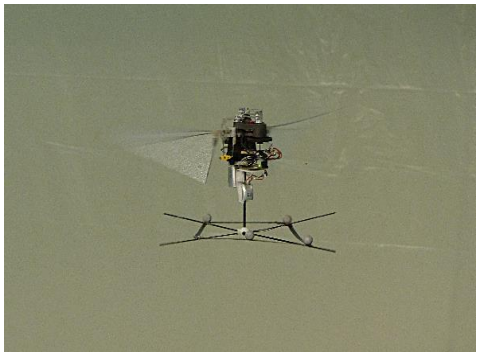

Figure 1. Robotic Hummingbird in stable hover.

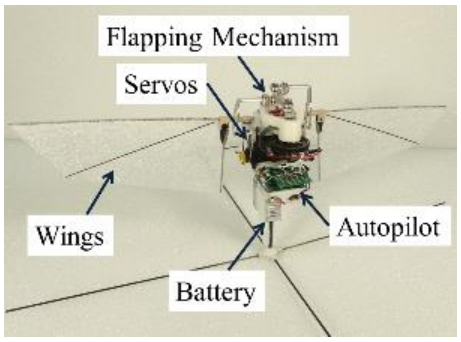

Figure 2. Hover-capable Robotic Hummingbird. *Labeled parts of the current flapper design*

structure is designed to have a high strength to weight ratio for minimal empty weight and maximum structural integrity. The vehicle uses at C-10 2900 KV brushless outrunner motor operating at 12,000 – 14,000 RPM, and driving the flapping mechanism at a frequency of 20-25 Hz through a 9.3:1 reduction gear. The wings are specially designed after extensive testing to generate the most lift at the lowest operational frequency, as well as be as light as possible in order to reduce in-plane inertial forces during flapping, but also to be strong enough to lift the weight of the vehicle (see Ref. 9). The final wing weighs only 0.8 grams, and is made of a simple carbon fiber frame and a 1/32'' flexible foam membrane which allows the wing to passively pitch under inertial and aerodynamic forces and assume a shape that maximizes the coefficient of lift of the wing.

Motivation for the Present Study

Much of the effort gone into the robotic hummingbird has been on the design, building, and successful flight tested of the vehicle, with much room for improvement in lift generation and energy consumption. Hence, this project was designed to aid in optimizing and improving the efficiency of the robotic hummingbird to demonstrate its superior maneuverability and gust tolerance in indoor and outdoor environments. To achieve this, the first step is to understand the fundamental aeromechanics of the flexible flapping wing used on the vehicle while at operational flapping frequency. This requires vertical force measurements, wing deflection measurements and inertial load separation through digital image correlation (DIC) techniques, and aerodynamic flowfield measurements through particle image velocimetry (PIV). These will be used to guide improving the wing design, and quantifying the system efficiency.

CHAPTER II

METHODS

To test the selected performance parameters of the robotic hummingbird, a series of experiments were conducted in which the instantaneous flap angle, lift, torque, and current were measured at a sampling rate of 1000Hz using an NI data acquisition device and LabVIEW program. From these measurements, the angular velocity was derived for mechanical power output and system efficiency calculations. The key parameters which were varied during the experimental process were the flapping frequency and flapping amplitude.

For the DIC experiments, the wing was painted with a black and white speckled pattern from which the software tracked the deflection relative to a zero motion reference image. Two Phantom micro 310 cameras capture 3D stereoscopic images simultaneously with the flash of a xenon strobe. The cameras were positioned such that their focal planes ran spanwise and along the length of the wing. The triggering was determined by a pre-selected shaft encoder output voltage. For the PIV experiments, the wing was painted black to absorb reflections from the laser and the room was filled with tiny smoke particles. A single Nikon Imager sCMOS was used to capture two images with a known time delay, and a dual pulsed Nd:YAG 532nm laser illuminated the smoke particles in the interrogation plane. The triggering to flash the camera and laser were done the same as for the DIC. The laser was positioned to "cut" the wing at the 70% spanwise location and the camera view was orthogonal to this. For both DIC and PIV, 50 images were captured for each flap angle, outliners were removed, and the remaining images averaged for a final measurement.

Description of Experimental Setup

An experimental setup was designed which replicated the wing kinematics on the rbotic hummingbird by utilizing the same extended four-bar crank rocker mechanism. A duplicate of the wing used on the vehicle was created for the experiment. Additionally, the same brushless motor as is used on the vehicle was also implemented in the experimental setup for flapping. The experimental setup flapped just a single wing (refer to figure 3 and 4). The rotational speed of the motor and thus the flapping frequency was governed by a brushless motor controller.

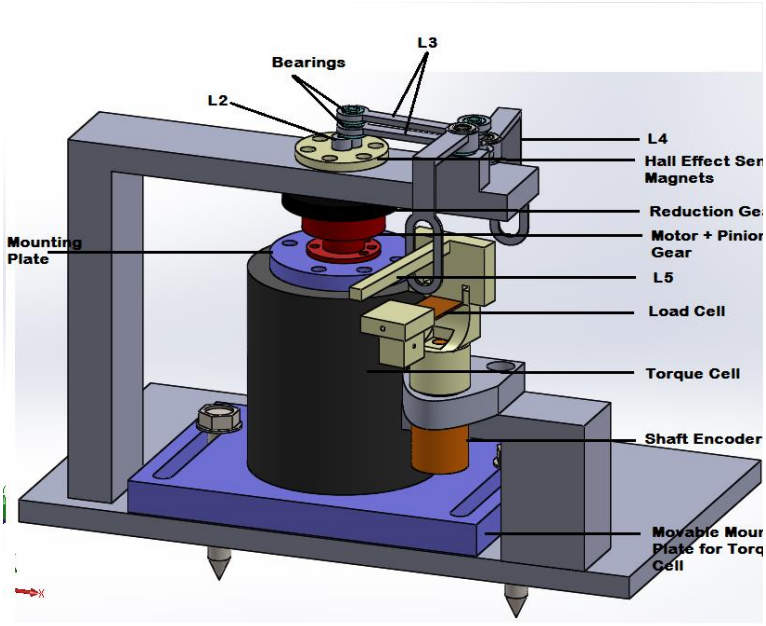

Figure 3. Labeled Solidworks Model of Experimental Setup. *Labeled parts indicate various sensors and features incorporated in setup*

Figure 4. Picture of Experimental Setup.

Sensors

To measure the instantaneous lift, torque, current, and flap angle, a variety of sensors were incorporated into the experimental setup . The list of sensors is as follows:

Shaft Encoder

A shaft encoder was used to measure and record the angular position of the wing at every instant in time during the flapping stroke. This data for angular displacement was differentiated later to obtain instantaneous angular velocity.

Beam Sensor

A beam sensor was used to measure the forces responsible for causing deflections of the wing in the z-direction. It was connected to the leading edge spar of the wing between the wing and wing mount: thus all aerodynamic and vertical inertial forces experienced by the wing were measured.

Torque Sensor

A torque sensor was used to measure the shaft torque output of the motor. It was mounted on a movable mounting plate under the motor. The collected data for torque included torque output due to drag, inertial loads, and friction. It was used to calculate instantaneous mechanical power output and estimate the system efficiency.

Shunt Resistor

A shunt resistor was used to calculate the instantaneous current by measure the instantaneous voltage drop and dividing it by the shunt resistance which was 0.004Ohms +/- 0.5%. This resistor was connected in series with the ground of the motor electrical system during the flapping motion and were used to obain the instantaneous electrical input power.

DIC and PIV Setup

For the DIC and PIV experiments, the same flapping wing rig was used, except that the entire experimental setup shown in Fig. 3 and 4 was mounted onto a rotating platform with a rotation axis concentric with the flapping axis. This allowed the reference frame of the wing to be rotated relative to the fixed reference frame of the camera and laser system. This permitted interrogating the wing for deflection and flowfield measurements at discete flap angles and the results interpolated for a complete non-dimensional stroke time history of these quantites as needed.

Experimental Procedure

The flapping amplitude of the robotic hummingbird is a significant parameter that determines the amount of lift produced, and since changing the flapping amplitude changes the flapping kinematics the power drawn from the battery varies. At the same time, the larger the amplitude for a given thrust, the lower the disk loading and the higher the aerodynamic efficiency. Thus a balance needed to be found between the amount of battery life needed and the flapping kinematics that would optimize lift generation with respect to power drawn. To find the optimum value of these flapping paramters, experiments were conducted across a range of frequencies varying from 10 Hz to 20 Hz at intervals of 2.5 Hz and a range of amplitudes varying from 98 degrees to 135 degrees. The flapping amplitude was changed by modifying the position of the wing rotation axis with respect to the linkage contact point. For larger amplitudes such as 135 degrees, tests were conducted only up to 15 Hz since beyond this frequency the amount of lift generated exceed 30g which led to mechanical issues with the bench-top setup.

For each frequency and amplitude, the flap angle, current, vertical force, and torque output of the motor were instantaneously measured. The procedure for obtaining the data involved first collecting "zero" data for 10 seconds, which provided the reference values for the force and torque measurements. Next, the flapping frequency was increased from 0 Hz to the desired flapping frequency and held constant for 10 seconds. Finally, the frequency was returned to 0 Hz, and another 10 seconds of "zero" data was collected. The average of both the "zero" values became the final reference values. This systematic experimental procedure allowed for good data collection.

The deflection of the wing and the aerodynamic features are of greatest interest at the operational frequency of the robotic hummingbird 20 Hz; therefore the deflection and flowfield were measured at this frequency. However, due to the very large deflections at 20 Hz, the software was unable to correlate between the zero motion reference and the deflected shape. For this reason, the deflections were calculated at 13 Hz and 17 Hz as well as 20 Hz, and the total deflection was determined from sequential displacement calculations from 0 to 20 Hz. The deflection was captured for flap angles in increments of 10° from -55° to 55° (0° being the mid-stroke). If a significant amount of difference in the deflection between two adjacent measuremnts was observed, measurements were taken in finer steps as needed. For the PIV experiments, 10° increments were found to be sufficient to capture the key flowfield features.

CHAPTER III

RESULTS

Once the data was collected, a number of post-processing functions were applied to the data in order to determine trends and analyze and the relationship between performance. The first step in the post processing analysis was to apply a Fast Fourier Transform (FFT) to the data to convert it to the frequency domain. The amplitude-frequency graphs were plotted for the different data sets in order to (1) verify that the flapping frequency was held for he duration of the experiment, and (2) select the optimum cut-off frequency factor for data filtering procedures, which for these experiments was 3 times the flapping frequency. The second step in the process was to cut the data into discrete cycles and overlay each time history plot to determine the consistence of the force, torque, and flap angle data during the test. This was done by following the curve of the flap angle data, and cutting the data at end of the upstroke and beginning of the downstroke. Finally, with the measured time histories overlaid, a final time history average was calculated for each of the measurement quantities.

For the deflection measurements, the wing speckled pattern was used to generate a grid which overlaid the wing, and the deflection measurements of each of the grid points, or wing subparticles was then calculated. Since the goal of the deflection measurements was to both quantify the shape of the wing and calculate the inertial forces, a specialized MATLAB® code was written which first interpolated the deflection results to generate a non-dimensionalized stroke time history of each of the wing subparticle displacements. From these, the velocity and acceleration was derived and the total inertial force in the veritical direction was calculated by

multiplying the time history of each of the wing subparticles by their respective masses and summing the total. Second, the post-processing code extract the camber and twist from the deflection measurements and was used to quantify the shape of wing at selected non-dimentional stroke times.

Kinematic Measurements

The angular displacement produced by the single flapping wing was measured using the shaft encoder. The instantaneous angular displacement across a range of frequency tests at a fixed amplitude was considered and compared. As expected, as frequency increased, the time histories of the angular displacement remained the same. This agrees with the hypothesis since the kinematics of the flapping motion should remain the same for any frequency for all other parameters fixed. This result further demonstrates that flapping amplitude remained consistent from one experiment to another. Additionally, the shaft encoder data was then differentiated to find the instantaneous angular velocity of the wing, which was found to increases as frequency increases since the same flapping motion as expected.

Vertical Force Measurements

The force produced by the single flapping wing in the vertical direction was measured using the beam sensor connected between the wing and wing mount. After running several tests at each frequency, the overall average time history of the instantaneous forces across tests of selected frequencies were considered. In figure 5, these average instantaneous forces are plotted together on the same graph for comparison puproses. From these results, it can be seen that as frequency increases, average vertical force increases. This agrees with the hypothesis since

increase in frequency leads to an increase in angular velocity which ultimately results in increased lift. However, it can be noted that there is a significant amount of negative force measured during the transition from upstroke to downstroke for the higher frequencies, especially at 20 Hz. One possible explanation is that the motion of the structure produced significant negative inertial loads during this time. The second observation from this results is that the vertical force is almost symmetric for the forward sweep and backward sweep, and experiences a spike in magnitude during the mid-stroke when angular velocity is maximum, which is what is expected.

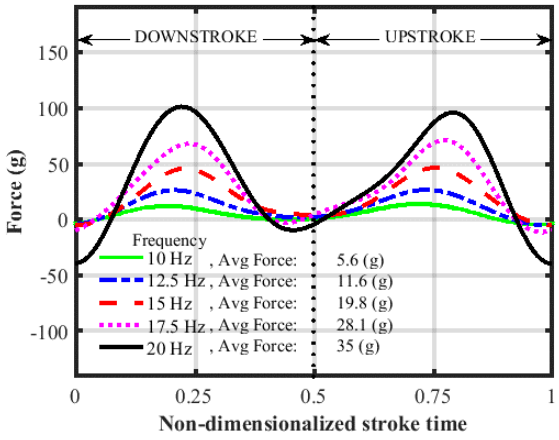

Figure 5. Instantaneous vertical force at selected frequencies.

Assuming quasi-steady flow, the squared angular velocity calculation is used in calculating a coefficient of lift for the wing, valid for regions in which the square angular velocity is non-zero. Using equation (1), this is calculated as follows:

$$C_L = \frac{L_{avg}}{\frac{1}{2} * \rho * V_{avg}^2 * J} \qquad (1)$$

Where J, the second moment of area, is calculated using equation (2), and equations (3a) and (3b), as follows:

$$J = \int C(r) \cdot r^2 \cdot dr \qquad (2)$$

$$C(r) = m_1 \cdot (r - WS_1) + C_{max} \quad for\ 0 < r < WS_1 \qquad (3a)$$

$$C(r) = m_2 * (r - WS_1) + C_{max} \quad for\ WS_1 < r < WS_2 \qquad (3b)$$

The instantaneous vertical force coefficient calculated based on this equation is shown in Figure 6 plotted for selected flapping frequencies on the same graph for comparison purposes. These results isolate the effect of velocity on the vertical force, and allow analyzing just the lifting qualities of the wing based on its instantaneous shape. In figure 6, the regions in which the force coefficient calculation is valid is approximately 0.15s to 0.4s for the downstroke, and 0.65s to 0.9s for the upstroke. This is because the vertical force during other times are relatively small and therefore insignificant. These results show very large force coefficents for the entire range of flapping frequencies, much higher than those calculated for similarly sized flapping rigid wings in hover (Ref 3). Additionally, the fact that the wing experiences higher lift coefficients at lower flapping frequencies during the first half of the upstroke indicates that possibly a more graduate acceleration up to speed generates a more controlled wing deflection shape, and thus better lift coefficients.

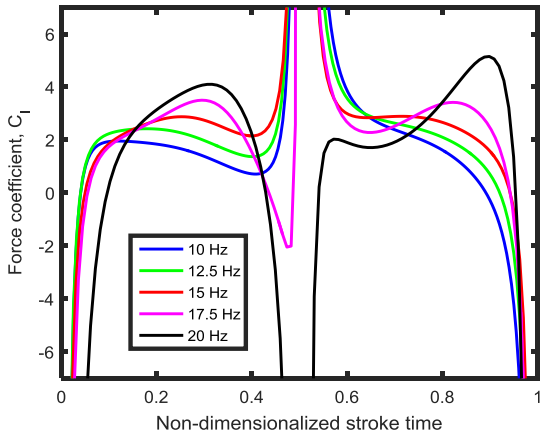

Figure 6. Calculated instantaneous coefficient of vertical force at selected frequencies.

Torque Measurements

The mechanical torque generated by the motor for driving the single flapping wing was measured using the torque sensor on which the motor was mounted. In figure 7, the final average

time history of the instantaneous torque was plotted for different flapping frequencies for comparison purposes. It can be seen that as frequency increases, average torque increases. Additionally, the range of torque produced during increases as well as the mean offset from zero. This can lead to to large variations in the motor's mechanical output, which effects the efficiency calculations. This increase in torque occurs due to the increase in in-plane inertial forces which are proportional to acceleration, and aerodynamic drag at higher operating frequencies. Also, the torque is almost symmetric for the downstroke and upstroke, and experiences a spike in magnitude right before the stroke ends. This is where the combination of acceleration-induced inertial forces and aerodynamic drag are the greatest. Since the peak torque does not occur at exactly the end stroke where inertial forces are the largest, this means the in-plane forces are not completely dominated by inertial loading, but that aerodynamic loading is also equally substantial.

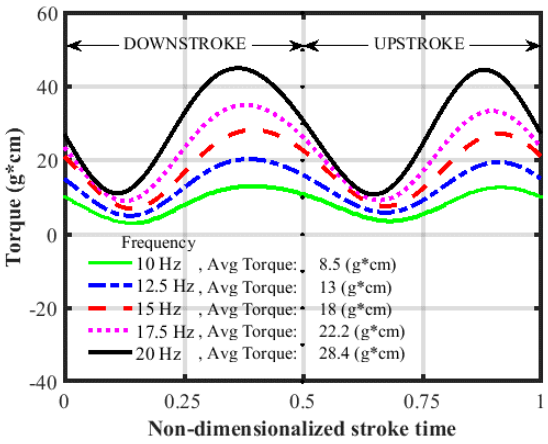

Figure 7. Instantaneous torque at selected frequencies.

In order to calculate the mechanical power output, the measured torque is multiplied by the angular velocity of the motor, as seen in equation (4).

$$P_{out} = T_{avg} \cdot GR \cdot f \qquad (4)$$

Furthermore, the electrical power input was calculated using equation (5) and the efficiency was calculated using equation (6) (See figure 13(c)).

$$P_{in} = C_{avg} \cdot V_{in} \quad (5)$$

$$E = \frac{P_{out}}{P_{in}} \cdot 100\% \quad (6)$$

Results of Amplitude Testing

Having established the validity of the experimental measurements, the amplitude of the flapping motion was now changed across selected frequencies by changing the distance between the rotation axis of the wing and the rotation axis of the final linkage which effectively changed the contact point between L4 and L5 (see figure 3). For these experiments, four amplitudes were

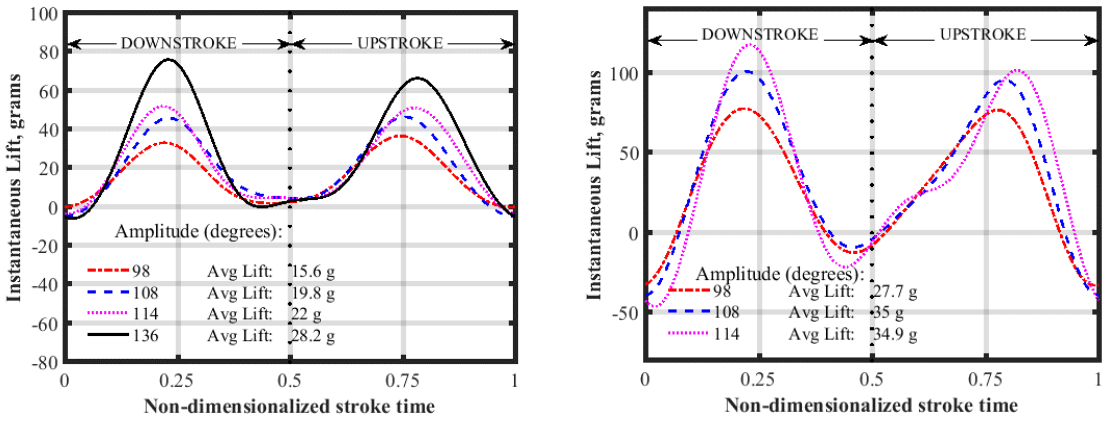

Figures 8 (a), (b) – Instantaneous Lift for a given Flapping Frequency (15 and 20 Hz) for a range of flapping amplitudes.

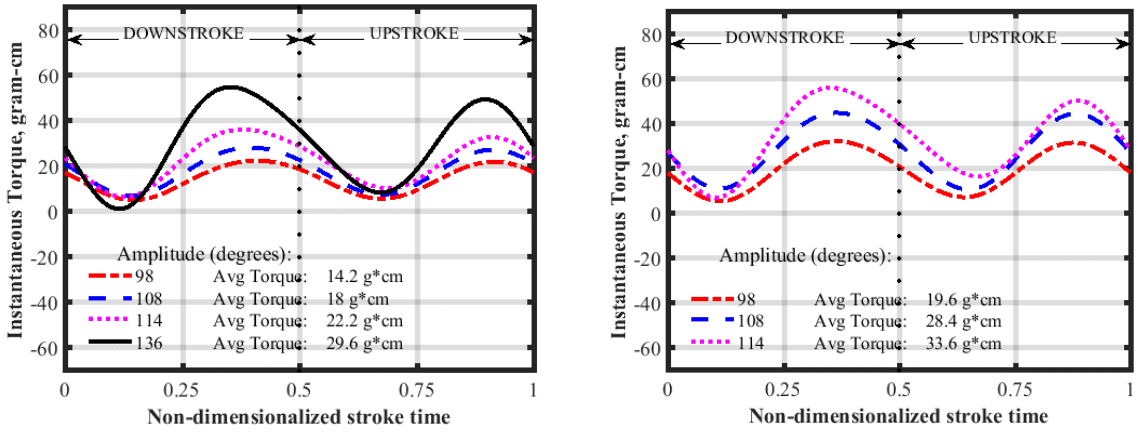

Figures 9 (a),(b) – Instantaneous torque for a given Flapping Frequency (15 Hz (a) and 20 Hz(b)) for a range of flapping amplitudes.

tested: 98°, 108°, 114° and 136°. As expected, these results show that the maximum lift was achieved at mid-stroke whereas maximum mechanical power was drawn close to the stroke ends, and that as frequency was increased, the average lift increased too (figures 8(a),(b)). Additionally, as the amplitude was increased, the amount of motor shaft torque at a given frequency increased as well (figures 9(a), (b)). This indicates that a larger amplitude requires a larger supply of mechanical power output thus reducing the system efficiency, most likely due to the higher wing speeds and larger accelerations.

When comparing the average lift generated with respect to flapping frequency for a range of amplitudes, it was found that there was an overall positive trend as expected from previous studies (see fig 10(a), Ref 9). Additionally, the average lift produced per unit squared amplitude is approximately a constant linear relationship across the range of selected frequencies for all tested

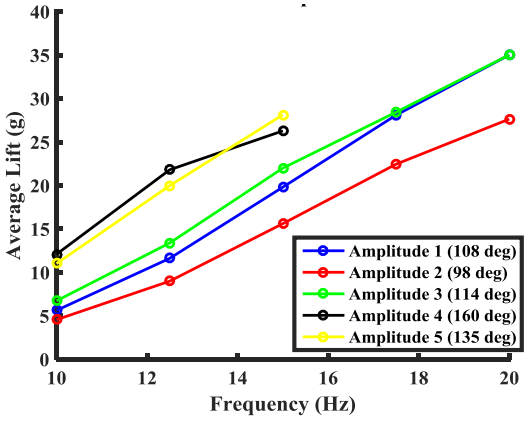

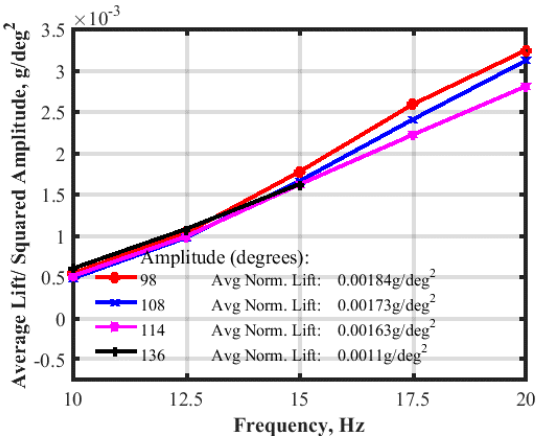

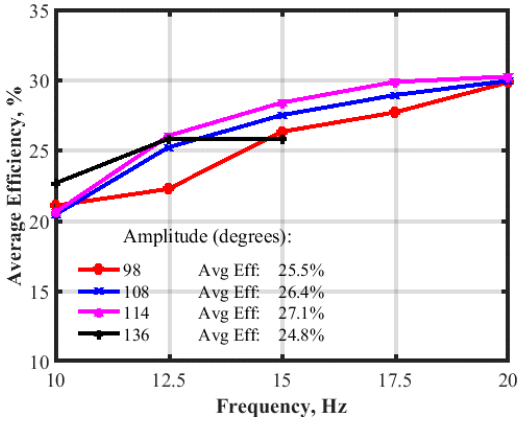

Figure 10(a) – Average lift generated at selected flapping frequencies for a range of flapping amplitudes.
Figure 10(b) – Average lift generated per unit squared amplitude at selected flapping frequencies and amplitudes.
Figure 10(c) - Average efficiency at selected flapping frequencies for a range of flapping amplitudes

amplitudes (see fig 10(b)). It is of interest to note that the average amount of lift generated per unit squared amplitude decreases as amplitude increases across all frequencies, indicating that the wing is more efficient in producing lift at lower flapping amplitudes. It is also interesting to note that the differences in lifting performance become more prominent at higher frequencies, indicating that lift can be generated more efficiently by increasing the flapping frequency at lower flapping amplitudes such as 98 or 108 degrees, rather than increasing the amplitude at a lower flapping frequencies.

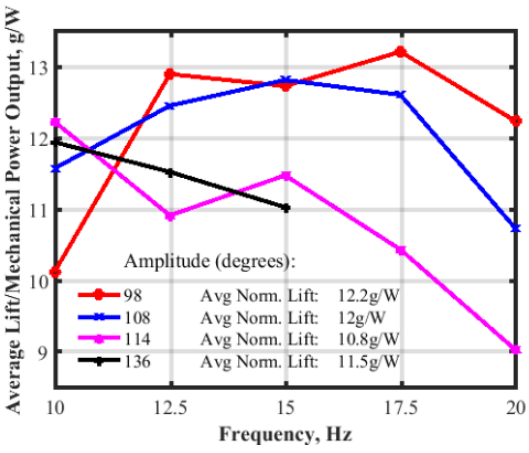

Figure 11. Average lift normalized by average power output at selected flapping frequencies for a range of flapping amplitudes.

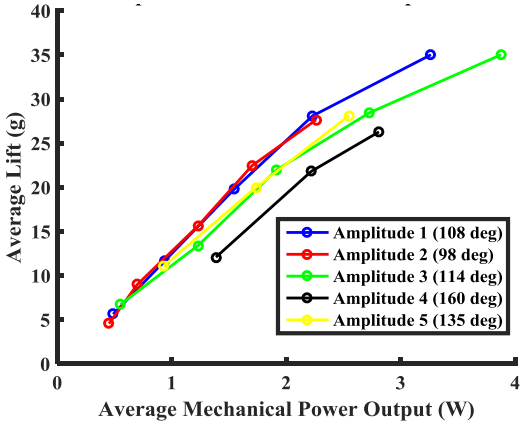

Figure 12. Average lift generated for a given average mechanical power output at selected flapping frequencies and amplitudes.

In addition to producing an increased amount of lift, these large amplitudes drew tremendous amounts of power. As seen in figure 11, the average lift generated per unit mechanical power output decreases with increased flapping amplitude. Additionally, figure 12 demonstrates how for a given amount of electrical power input or mechanical power output, the amount of lift generated increases substantially with decreasing amplitude. Thus, based on these quantitative power loading results, the overall effect of increasing amplitude beyond 110 degrees at high flapping frequencies was found to be

quite inefficient. Hence, from a system efficiency perspective, an optimum flapping amplitude of 108 degrees was found experimentally.

Effect of Study on Improving Robotic Hummingbird Flight

These results have shown that the current amplitude and frequency combination utilized on the robotic hummingbird is very near the optimal. However, the instantaneous current drawn by the motor, having never before been measured, showed a dramatic difference in the mean and peak current outputs. Although the average current was well within the maximum output current of the existing brushless motor controller threshold which was 6 amps, the peak current values exceeded the maximum output significantly. This helped to explain speed controller failure and overheating during test flying. Based on this result, the motor controller on the robotic hummingbird was upgraded to a controller capable of 10 amps of current output. This resulted in much lower operating temperatures and helped prevent the controller from burning out during flights, which increased the flight time and quality of the robotic hummingbird.

Inertial Calculations and Deflection Measurements

Using the digital image correlation post-processing code described above, the time history of the inertial forces was calculated and subtracted from the total force measured from the beam sensor, and these are plotted in figure 13. These results are important, since they are the first time vertical inertial

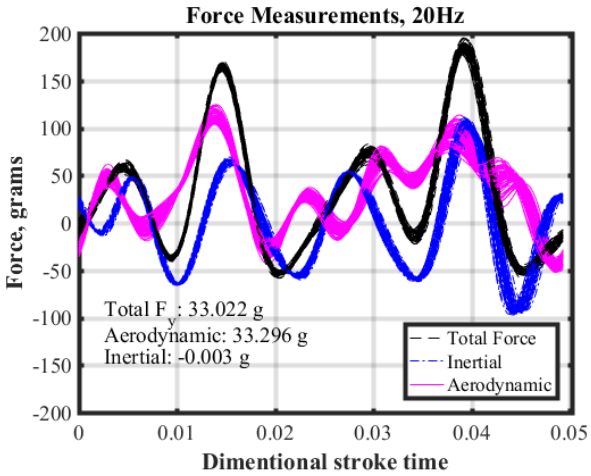

Figure 13. Summary of vertical forces acting on the wing during flapping. Aerodynamic forces are equal to total minus inertial.

forces have been calculated for a flapping flexible wing. Although there does not yet exist a computational result to serve as a sanity check, intuitively, the results are as expected. At times during the stroke when the wing is generally moving upwards, the inertial force is in the negative direction, and vice-versa. Additionally, the sum of the total inertial force in the vertical direction is zero.

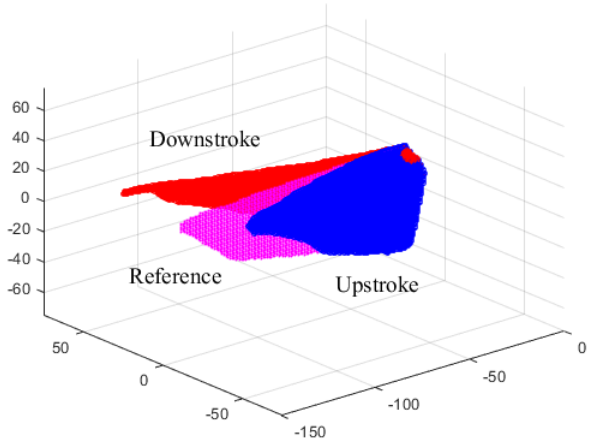

Figure 14. 3-D displacement results from DIC measurements for midstroke position during upstroke and downstroke.

The wing geometric pitch angle along the span is an important measurement result of the DIC experiments and can be extracted from the deflected shape (example shown in Figure 14). For select locations during the downstroke motion, the pitch angle, which is defined as the angle between the chordline and horizontal, is plotted along the wing in Figure 15. Note the relatively high degree of twist along the span of the wing, and the flairing upwards towards the tip.

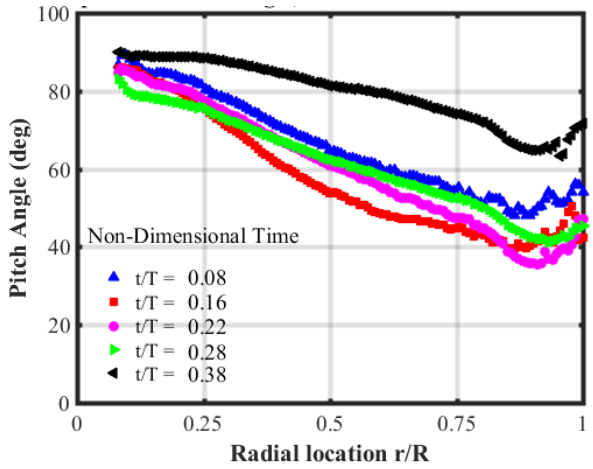

Figure 15. Pitch across wing span during downstroke for selected non-dimensional stroke times.

Flowfiled Measurements

The flowfield and aerodynamic structures at the 70% spanwise location were resolved using the particle image velocimetry techniques described above. Measurements were taken at discrete flap angles (non-dimensional stroke times) during the dowstroke motion of the wing, and the results were plotted with background vorticity shading to reveal the development of leading, trailing, and starting vortices (Fig 16 a-f).

From these plots, the development of the starting vortex satisfying Kelvin's circulation theorem is clear. Aditionally, of interest to note is the fact that early in the flap cycle when the angle of attack is very high, the flow is still attached to the wing due to dynamic stall effects in unsteady flow conditions, and explains the high lift coefficient. The development of a strong leading vortex begins just before mid-stroke, and grows to a diameter the length of the wing chord at the 70% span; at a non-dimensional stroke time of about 0.4s, the vortex burst.

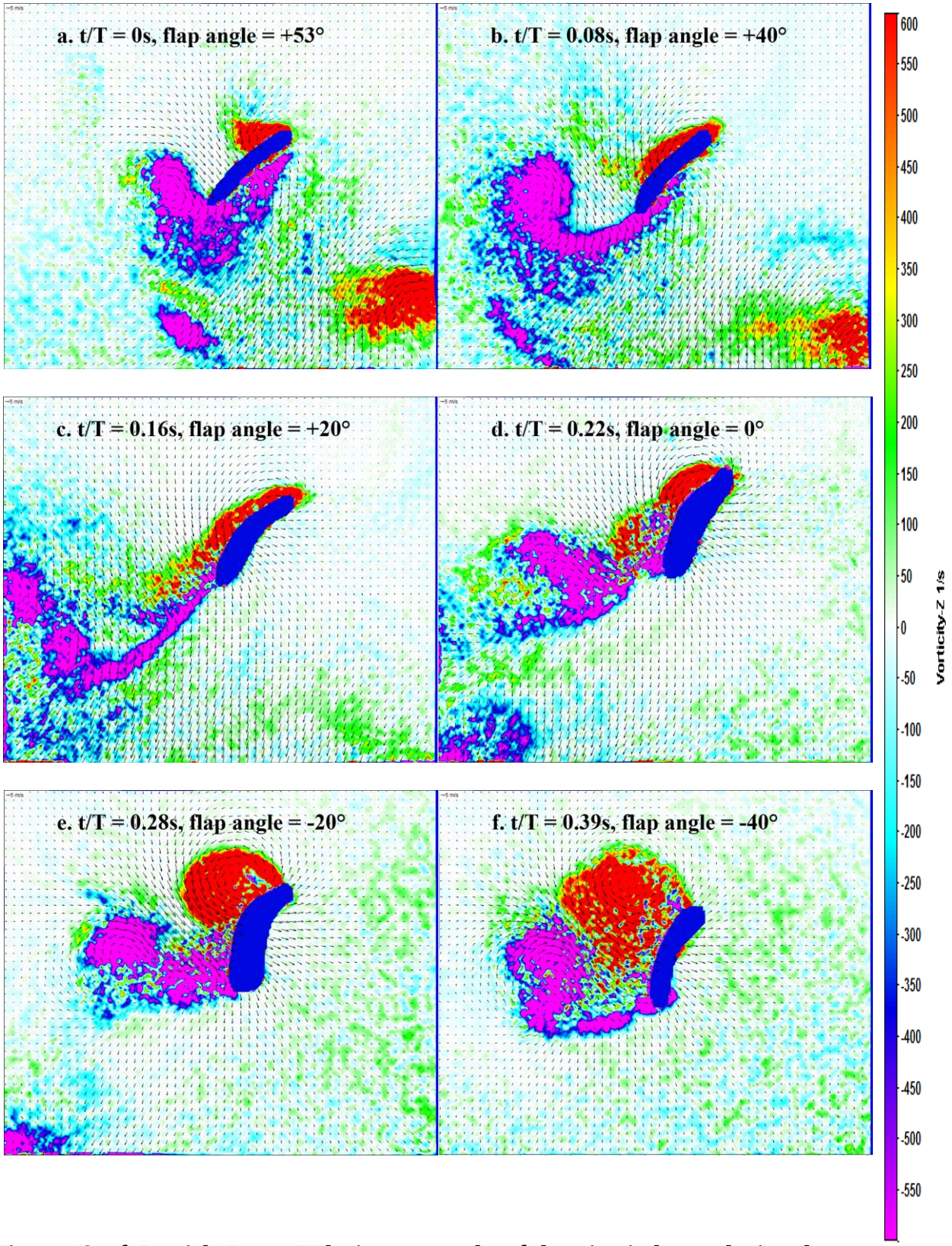

Figure 16 a-f. Particle Image Velocimetry results of the wing in hover during the downstroke.

CHAPTER IV

CONCLUSION

This study marks a key point in the aeromechanical characterization of flexible, hover-capable flapping wings. Systematic experiments have quantified instantaneous lift and torque, wing deflection during flapping, and important flowfield features. The experiments have (1) showed that a flapping amplitude of 108° is the best for system efficiency; (2) established a method for calculating vertical inertial force with physically sound results; and (3) revealed attached flow on the flexible flapping wing at high angles of attack which may explain high lift coefficients. These results are key in refining the design of state-of-the-art flexible flapping wings for use on the robotic hummingbird.

REFERENCES

[1]Vance, J. T., Faruque, I., and Humbert, J. S., "Kinematic Strategies for Mitigating Gust Perturbations in Insects," *Bioinspiration and Biomimetics*, Vol. 8, No. 1, 2013.

[2]Ansari, S. A., Zbikowski, R., Knowles, K., "Aerodynamic Modelling of Insect-Like Flapping Flight for Micro Air Vehicles", *Progress in Aerospace Sciences*, Vol. 42, 2006, pp. 129-172.

[3]Benedict, M., Coleman, D., Mayo, D., and Chopra, I., "Force and Flowfield Measurements of a Rigid Wing Undergoing Hover Capable Flapping and Pitching Kinematics in Air at MAV-Scale Reynolds Numbers," 54th AIAA/ASME/ASCE/AHS/ASC Structures, Structural Dynamics, and Materials Conference, Boston, MA, April 2013.

[4]Gerdes, J. W., Gupta, S. K., and Wilkerson, S., "A review of bird-inspired flapping wing miniature air vehicle designs." *ASME Journal of Mechanism and Robotics*, 4(2), 021003.1-021003.11, 2012.

[5]http://www.festo.com/cms/en_corp/11369.htm

[6]de Croon, G. C. H. E., Groen, M. A., De Wagter, C., Remes, B., Ruijsink, R., van Oudheusden, B. W., "Design, Aerodynamics and Autonomy of the DelFly", *Bioinspiration and Biomimetics*, Vol. 7, Num. 2, 2012.

[7]Ratti, J., "QV: the quad winged, energy efficient, six degree of freedom capable micro aerial vehicle," PhD dissertation, Georgia Institute of Technology, April 2011. http://hdl.handle.net/1853/44695

[8]Keennon, M., Klingebiel, K., Won, H., Andriukov, A., "Development of the nano hummingbird: A tailless flapping wing micro air vehicle", 50th AIAA Aerospace Sciences Meeting. January 2012, pp. 2012–0588.

[9]Coleman, David, Moble Benedict, and I. Chopra. "Design, Development and Flight-Testing of a Robotic Hummingbird." *71st Annual Forum of the American Heli. Society, Virginia Beach, VA*. 2015.